ELSEVIER

Journal of Structural Geology 29 (2007) 1650–1664

JOURNAL OF STRUCTURAL GEOLOGY

www.elsevier.com/locate/jsg

Kinematics of a kilometric recumbent fold: The Courel syncline (Iberian massif, NW Spain)

Francisco J. Fernández*, Jesus Aller, Fernando Bastida

Departamento de Geología, Universidad de Oviedo, J. Arias de Velasco s/n, 33005 Oviedo, Asturias, Spain

Received 10 January 2007; received in revised form 23 May 2007; accepted 31 May 2007
Available online 10 July 2007

Abstract

The Courel recumbent syncline is one of the best examples of a regional scale recumbent fold outcropping in the NW Iberian massif. A strain, microfabric and minor fold analysis of this structure has been integrated in an evolutionary model that begins with an episode of layer shortening, buckling and body rotation associated with deformation dominated by simple shear. Subsequently, the fold was flattened by dominant irrotational strain with maximum shortening perpendicular to the axial surface and maximum stretching parallel to the fold axis. This occurred during the first phase of the Variscan deformation, and gave rise to a fold with an axial surface dipping moderately towards the hinterland (SSW). The recumbent character of the fold was increased during the third phase of the Variscan deformation, which produced a large-scale open structure with a subhorizontal limb.

Keywords: Recumbent fold; Kinematics; Strain analysis; Iberian massif

1. Introduction

Large-scale recumbent folds are common in the internal zones of many orogens. They have been mainly interpreted as occurring in tectonic compressive settings, though examples in other tectonic environments have been also described. Some recumbent folds show a relationship to low angle reverse faults that does not have a ramp–flat pattern (Rich, 1934), as is the case in the Helvetic nappes (Dietrich and Casey, 1989). Several theoretical models have been proposed for the formation of recumbent folds. Most of these models combine simple shear deformation with shortening perpendicular to the shear plane (e.g. Sanderson, 1982; Ramsay et al., 1983; Ez, 2000). The Courel recumbent syncline in the northern Iberian massif is one of the most spectacular recumbent folds in the Variscan orogen.

The aim of this study is to create a kinematical model for the Courel recumbent syncline through the integration of all structures from the map scale to that of the optical microscope. Such modelling should shed some light on the conditions required for the formation of recumbent folds in general.

To gain insight into the folding mechanisms involved in minor folds associated to the Courel recumbent syncline, the program FoldModeler (Bobillo-Ares et al., 2004) was used. This geological software was developed using Mathematica™, and allows kinematic models of folds to be constructed and analysed in order to determine the strain on the theoretical fold profile. These models are developed by the successive or simultaneous superposition of strain patterns corresponding to several fold mechanisms. Comparison with strain features of natural folds can be used to gain insight into the kinematic mechanisms involved in their development. This software has been recently improved to allow the modelling of asymmetrical folds obtained by any combination of pure shear, simple shear, area change and rotation. This method has been combined with the study of quartz microfabrics and other techniques of structural analysis. In particular, a GIS has been used to perform grain shape and strain analysis of quartzite samples.

* Corresponding author. Tel.: +34 985 109545; fax: +34 985 103103.
E-mail address: brojos@geol.uniovi.es (F.J. Fernández).

0191-8141/$ - see front matter © 2007 Elsevier Ltd. All rights reserved.
doi:10.1016/j.jsg.2007.05.009

2. Geological setting

The Courel recumbent syncline is a kilometric scale fold located in the Ollo de Sapo domain of the Central-Iberian zone, near to the boundary with the Westasturian-Leonese zone (Fig. 1). These are two major zones of the hinterland of the Variscan belt in NW Spain and present a Palaeozoic succession more than 11,000 m thick with Cambro-Ordovician terrigenous series and minor calcareous intercalations, on top of which Silurian slates are found (Garganta beds in Figs. 2 and 3). Lower Devonian calcareous layers are found locally on top of the Silurian. In the Ollo de Sapo domain of the Central-Iberian zone, a Lower Ordovician porphyroid formation (Ollo de Sapo Fm.) appears at the base of the succession (Fig. 1).

In the Westasturian-Leonese zone and the Ollo de Sapo domain, the structural evolution of the Variscan deformation is characterized by three successive deformation phases. The first deformation phase (D_1) gave rise to close to tight folds strongly vergent to the foreland (Cantabrian zone, Fig. 1) and with an associated S_1 foliation (Matte, 1968; Marcos, 1973; Bastida, 1980). The Courel recumbent syncline has been interpreted as a D_1 fold (Matte, 1968; González-Lodeiro and Iglesias-Ponce de León, 1978; Martínez-Catalán, 1985). D_2 is responsible for thrusts and low dip shear zones with associated minor structures (Marcos, 1973; Bastida and Pulgar, 1978; Bastida et al., 1986). D_3 formed large-scale open folds that are upright or slightly vergent to the W and SW. These folds are approximately coaxial with the D_1 folds and have an associated crenulation cleavage in pelitic layers (Matte, 1968; Marcos, 1973; Pulgar, 1980). In the Serra do Courel the minerals that crystallize in the pelitic layers during the development of the different cleavages are quartz + chlorite + white

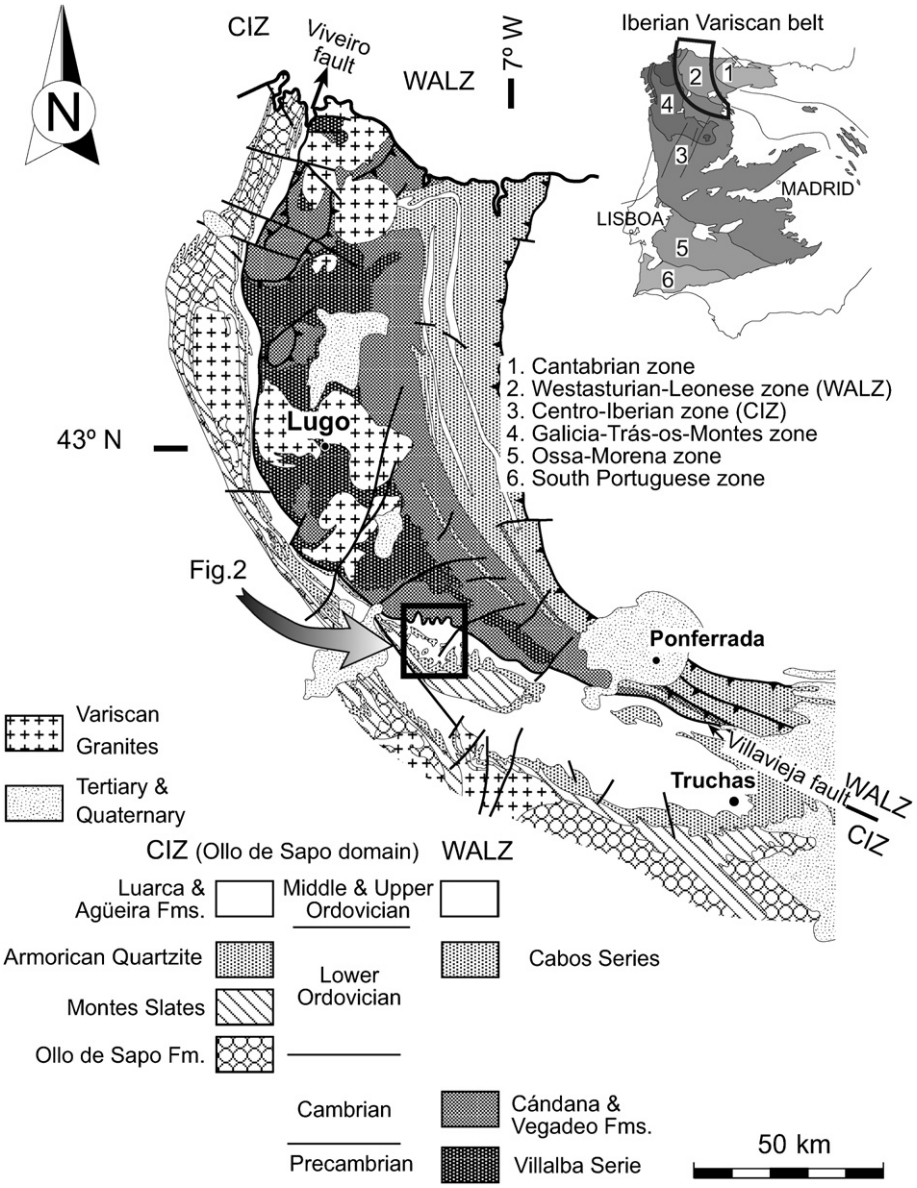

Fig. 1. Location of the study area in the Variscan NW Spain.

mica ± calcite, indicating metamorphic conditions of the green schist facies.

Another noteworthy structure is the Viveiro fault (Fig. 1). To the north of the study area, this fault dips to the west, trends N–S and has a normal dip-slip component greater than 11 km, together with a minor dextral strike-slip component (Martínez-Catalán, 1985; Martínez et al., 1996). To the south, this fault bifurcates, with the Villavieja fault forming the north-eastern branch (Fig. 1). The Courel recumbent syncline is located to the south of the Villavieja fault (Fernández, 2000, 2001) and both structures can be followed for more than 100 km. The Courel syncline is a recumbent fold in the study area, but laterally it changes its attitude as a result of later folding (Matte, 1968; Pérez-Estaún, 1978; Fernández, 2001).

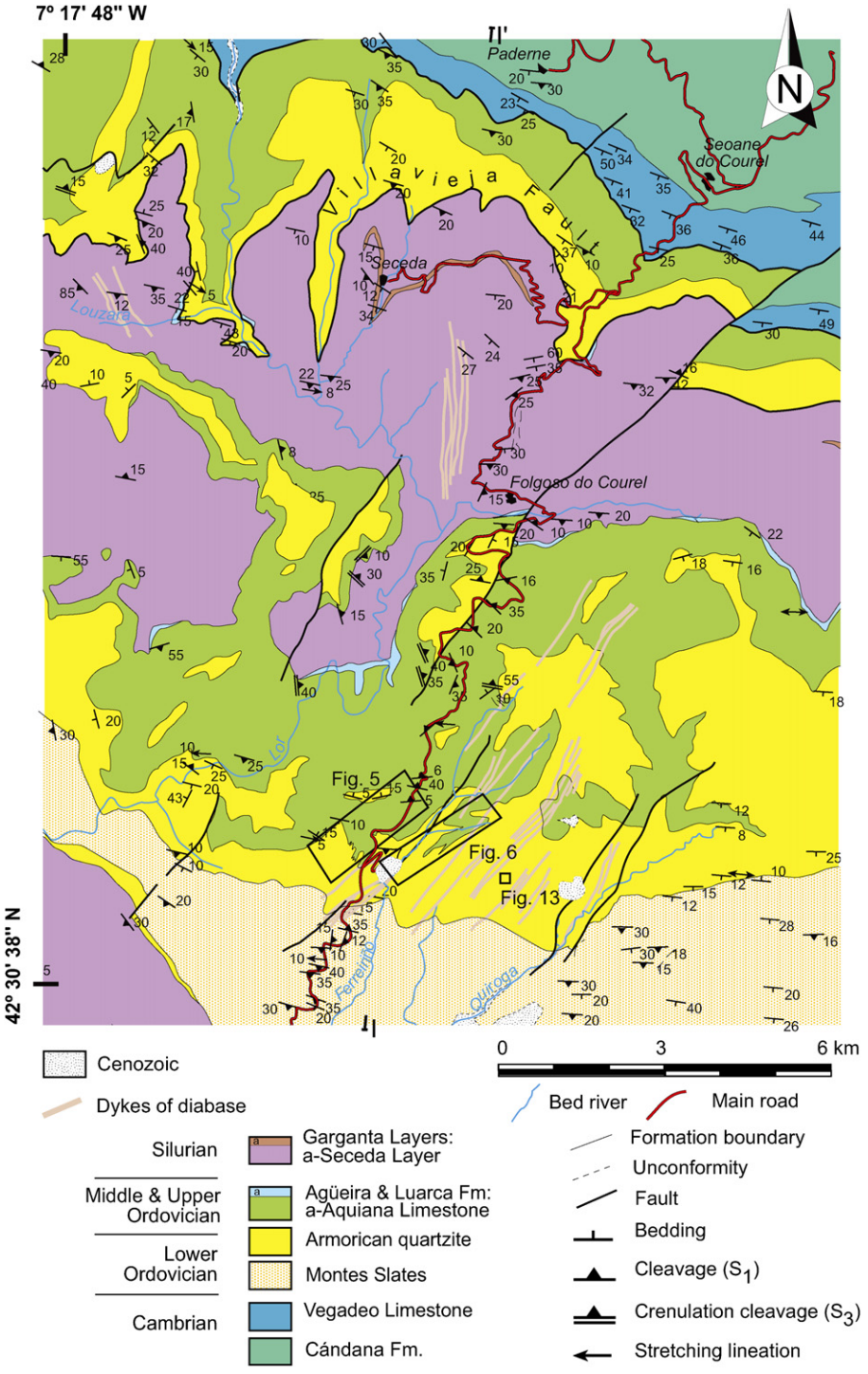

Fig. 2. Geological map of the study area. The cross section I–I′ is shown in Fig. 3. Sketches of the areas inside the squares are shown in Figs. 4 and 5. Mapping is based on Riemer (1963), González-Lodeiro and Iglesias-Ponce de León (1978), Abril-Hurtado (1979), Martínez-Catalán (1985) and unpublished data from D. Arias and the authors. See Fig. 1 for location.

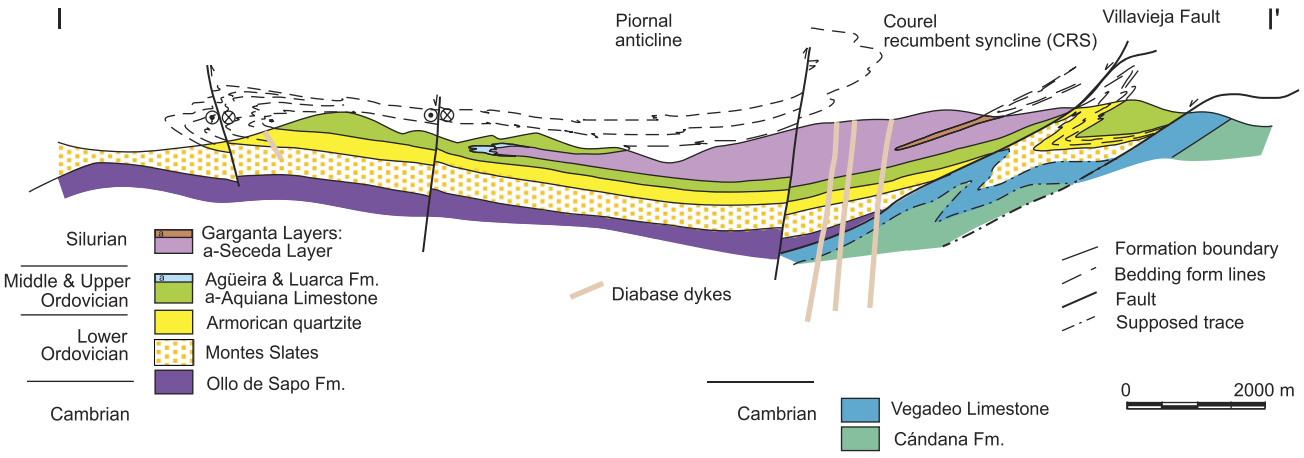

Fig. 3. Cross section through the central part of the Serra do Courel (trace shown in Fig. 2).

The Villavieja fault began its long history as an extensional pre-Variscan fault that controlled sedimentation from the Middle Ordovician to the Silurian. At this time a growth rollover anticline with thickened limbs developed in the hanging wall, to the south of the fault. In the crest of this anticline an Upper Ordovician calcareous succession (Aquiana limestones) was deposited, which changed towards the northern and southern limbs to a thicker siliciclastic succession (Luarca slates and Agüeira Formation). This structure greatly affected the geometry of the structures developed during the first deformation phase (Fernández, 2000, 2001).

3. Structural analyses

The first detailed geological map of the study area was made by Riemer (1963) and the first structural interpretation was made by Matte (1968). In this paper, and also in those of González-Lodeiro and Iglesias-Ponce de León (1978) and Martínez-Catalán (1985), the structure is interpreted as a pair of north vergent isoclinal folds: the Courel recumbent anticline (Matte, 1968) or Piornal anticline (Martínez-Catalán, 1985) and the Courel recumbent syncline, located to the north. A new geological map and cross section of the area are shown in Figs. 2 and 3.

D_1 folds have an associated slaty cleavage (Fig. 4) with an axial plane or slightly convergent pattern depending on the competence of the folded layers. Evidence of dissolution along cleavage seams is common. A weak stretching lineation, usually only observed under the microscope and defined by the orientation of quartz and/or chlorite crystals, appears on the S_1 planes in a direction parallel to the fold axes (Fig. 4). Boudins indicating extension in this direction are also present.

Minor D_1 folds are common near the hinge zone of the Courel recumbent syncline. They are type 1C folds (Ramsay, 1967). Protuberances in the hinge zone inner arc and wedge shaped veins in the hinge outer arc are observed in some of these folds indicating a mechanism of tangential longitudinal strain (Bobillo-Ares et al., 2000).

3.1. Microstructure and fabric analysis

The Armorican quartzite (Lower Ordovician, Figs. 2 and 3) has been sampled in several localities near the hinge zone of the Courel recumbent syncline (Figs. 2, 5 and 6). Under the microscope, all the samples have a grain size <200 μm and anhedral quartz dominates, with some chlorite and minor amounts of other phyllosilicates, plagioclase and opaque minerals. Moreover, acicular rutile, prismatic zircons and other inclusions are common inside the quartz crystals. S_1 is a domainal cleavage in the quartzite (Fig. 7) with cleavage domains defined by phyllosilicates and opaque minerals, and microlithons formed by polycrystalline aggregates of quartz and minor plagioclase. Cleavage domains vary from parallel to anastomosing (terms after Powell, 1979 and Borradaile et al., 1982).

The thin sections analysed were cut perpendicular to the foliation (plane *XY*) along the direction of the elongate quartz crystals (plane *XZ*), and normal to this (plane *YZ*). Fabrics observed are planar–linear (samples JB-1, 4, 5, 6, 7 and 8) or just planar (samples JB-2 and JB-3). Since all sections contain similar microstructures, the two samples with the maximum and minimum values of aspect ratio for the quartz crystals, JB-1 and JB-7, were selected for a quantitative analysis of the shape fabric. Fabrics were characterized using the capabilities of GIS for the analysis of forms, and the following data were obtained: grain size histograms, grain ellipticity (or aspect ratio), the angle (ϕ) between the major axis of the ellipse inscribed in each grain and the foliation trace, and the shape parameter (S = normalized area/square of the grain perimeter), which describes the irregularity of the grain boundary (Fernández et al., 2005). The results obtained are shown in Figs. 8 and 9a. *XZ* and *YZ* sections show similar grain size and a distribution with inequigranular–interlobate grains in which two grain populations have been distinguished (Fig. 8b): grains A with modal values of the diameters of circles with the same area ranging between 15 and 22 μm, and grains B in which these values are about 50 μm. Shape parameters for section *XZ* of the sample JB-7 are shown in Fig. 9a. The aspect ratio reaches maximum values of 7 for grains B, whereas the

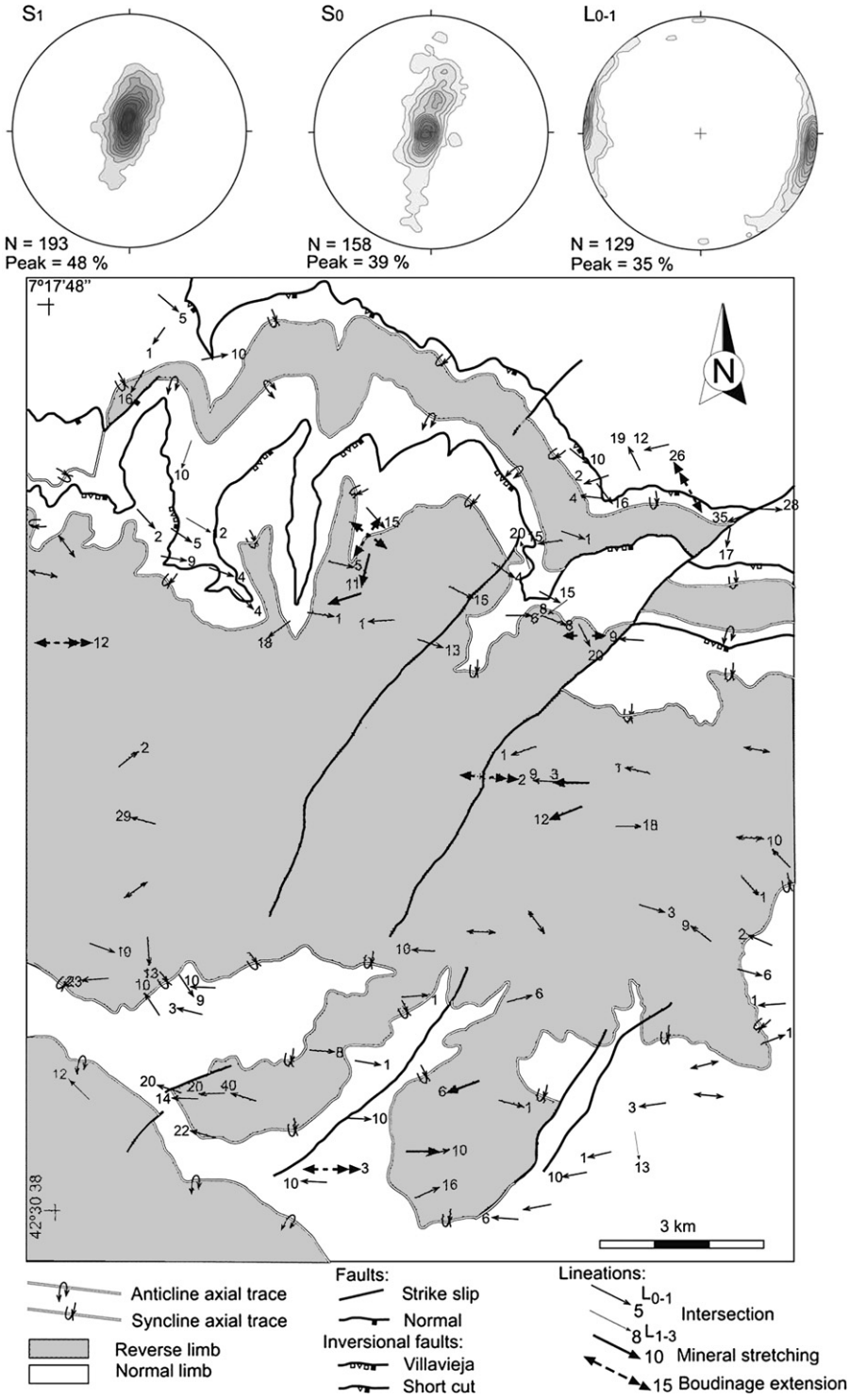

Fig. 4. Structural map of the study area showing the regional trend of L_1 (mineral lineation) and fold axes. All diagrams (S_0 surface poles, S_1 surface poles and L_{0-1}) are lower hemisphere equal-area projections. Reverse limbs are shaded.

maximum value is 3.5 for grains A. The preferred shape orientation of grains A is also less developed, and they also present a lower boundary irregularity ($S = 0.51$). The greater boundary irregularity of grains B ($S = 0.38$) is related to dynamic recrystallization by bulging (Fig. 7e and f), corresponding to regime 1 of Hirth and Tullis (1992). As a consequence, grains A are interpreted as having resulted from dynamic recrystallization.

3.2. Strain analysis

The R_f/ϕ method (Ramsay, 1967; Dunnet, 1969; Ramsay and Huber, 1983; Lisle, 1985) was applied on the *XZ* and *YZ* sections of samples JB-1 and JB-7, and the results have been contrasted using the TFry and ASPAS methods (Fig. 10; Fernández et al., 2005), based on the Fry (1979) method and

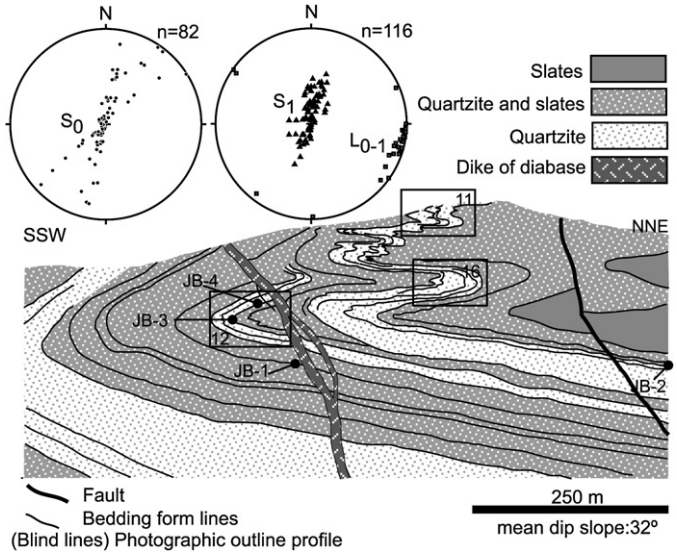

Fig. 5. Schematic sketch of the Convento slope section showing location of analysed minor folds and samples (face to west, location shown in Fig. 2).

the intercepted segments′ method (Exner, 1972), respectively. These methods have been improved using the capabilities of a GIS for the treatment of the spatial relationships between the points, lines and polygons that characterize tectonic fabrics (Fernández et al., 2005). In this analysis, the population of dynamically recrystallized grains (grains A), which represent 9% of sample JB-1 and 4% of sample JB-7, was not considered.

The diagrams obtained by the R_f/ϕ method are symmetrical for all sections (Fig. 10). The quartz grains show some initial ellipticity (R_i). The R_i curves, R_s values and best fit χ^2 parameters of the R_f/ϕ diagrams were calculated using the spreadsheet for finite strain analysis by Chew (2003). This program calculates the strain ellipse (R_s) by selecting the particular strain that yields the most random initial distribution of marker orientation. Distributions open at the base in the sections *YZ* indicate that $R_i > R_s$ in these sections (Fig. 10c) with R_s values of 1.20 (JB-7) and 1.31 (JB-1). Distributions observed for the sections *XZ* can be interpreted as open or closed at the base, as can be deduced from the contour density map of Fig. 9d. R_s values are 1.61 (JB-1) and 1.4 (JB-7). If it is assumed that $R_{imax} < R_s$, and R_{imax} is calculated by the method described by Ramsay and Huber (1983), in which the maximum and minimum values of the contour map are considered, the R_s value obtained for section JB-7 is 2.01. This value can increase to 2.71 if the maximum ellipticity is considered (as suggested by Lisle, personal communication), instead of the contour map, which artificially weighs up the maxima and minima.

R_s values obtained by the TFry and ASPAS methods compare well with those obtained with the R_f/ϕ method. Nevertheless, sample JB-1 has higher χ^2 values than the critical values given by Lisle (1985), suggesting that it was probably deformed in a manner other than that prescribed by the passive marker model, or that a pre-strain fabric was present. Since the fit to an ellipse is made in these two methods by a least squares method (Fernández et al., 2005), it can be tentatively suggested that this type of fit softens the ellipticity of the strain ellipse.

Using the mean R_s value obtained for each section from the three methods, and assuming isochoric deformation, it is possible to calculate $\sqrt{\lambda_1}$, $\sqrt{\lambda_2}$ and $\sqrt{\lambda_3}$ for each sample. The values obtained are 1.21, 1.13, 0.73 for JB-1 and 1.30, 1.01, 0.76 for JB-7.

3.3. Quartz c-axis fabrics

The fabrics of a quartzite from the Serra do Courel (sample GAE-9; Matte, 1968) were analysed using X-ray goniometry by Schmid et al. (1981), who interpreted them as formed at high temperature with activation of prism <*c*> slip, and development of a *c*-axis lineation parallel to an N–S oriented stretching lineation observed in the sample. These results were discussed by Bouchez et al. (1984), who argued that the N–S lineation defined by the elongation of quartz crystals (*X*q) in

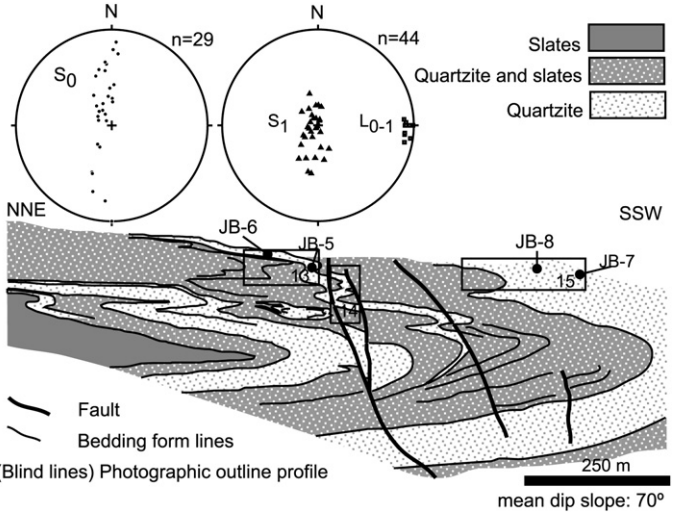

Fig. 6. Schematic sketch of the Peña Falcoeira slope section showing location of analysed minor folds and samples (face to east, location shown in Fig. 2).

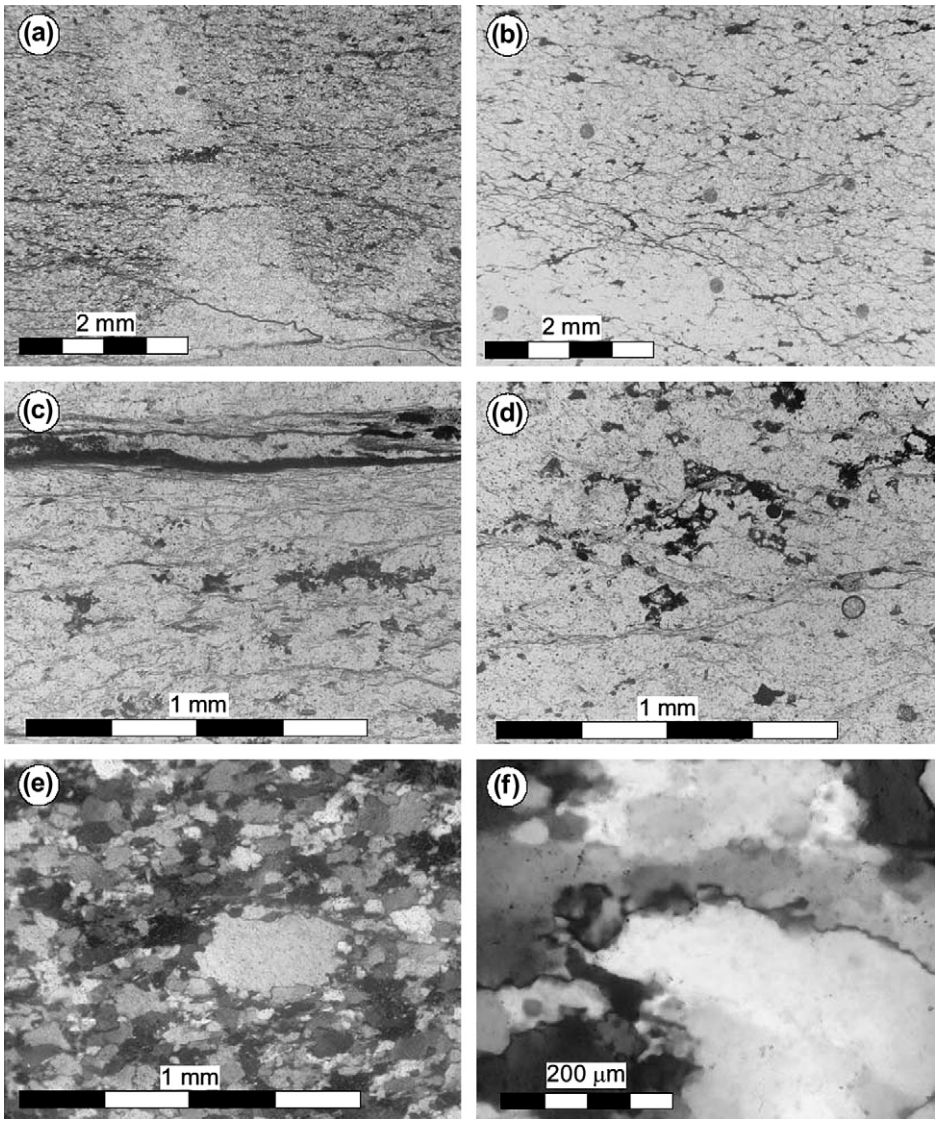

Fig. 7. Microphotographs of the Courel quartzite. (a) Domainal cleavage with alignment of opaque material penetrating inside a quartz vein. Section *XZ* of sample JB-1. PPL. (b) Rough foliation mainly defined by opaque material. Section *XZ* of sample JB-5. PPL. (c) Domainal foliation defined by fine-grained phyllosilicates (chlorite, muscovite). Section *XZ* of sample JB-3. PPL. (d) Domainal foliation in section *YZ*. Sample JB-2. PPL. (e) Polycrystalline quartz with irregular grain boundaries formed by grain boundary migration. Section *XZ* of sample JB-7. CPL. (f) Typical fabric of dynamic recrystallisation in large old quartz grains with irregular boundaries formed by bulging. Section *XZ* of sample JB-6. CPL.

sample GAE-9, was in fact a secondary fabric perpendicular to the maximum stretch (*X*) defined by the orientation of inclusions of acicular rutile and prismatic zircon in quartz. Moreover, Bouchez et al. (1984) found TEM microstructural evidences of activation of prism and basal slip in the $<a>$ direction, and also some rhombohedric slip in the $<c+a>$ direction. They interpreted these data as the result of the fabrics forming at low temperature.

The precise location of sample GAE-9 is not indicated in any published paper, and this hampers a comparison with the samples studied here, whose location is shown in Figs. 5 and 6. All the *XZ* sections analysed show a dominant orientation of the prismatic zircons parallel to the stretching lineation defined by the quartz crystals (*X*), with the formation of boudins in some cases, whereas in sections *YZ*, zircons do not show a prismatic shape and have a random orientation. The maximum stretch in all the samples (GAE-9 included) is parallel to D_1 fold axes and approximately E–W.

XZ and *YZ* sections of eight samples have been studied, and 150–300 quartz *c*-axes have been measured in each section using a U-stage. Data were then rotated to plot them together for each sample (Fig. 11). The fabrics have orthorhombic symmetry suggesting a mainly coaxial deformation in the last stages of the fabric evolution (Fig. 11). The fabrics of the overturned limb resemble the theoretical patterns obtained by Lister and Hobbs (1980) for their quartzite models B or C in plane strain conditions, whereas the fabrics of the normal limb show a slight tendency to flattening strain conditions, in agreement with strain measurements.

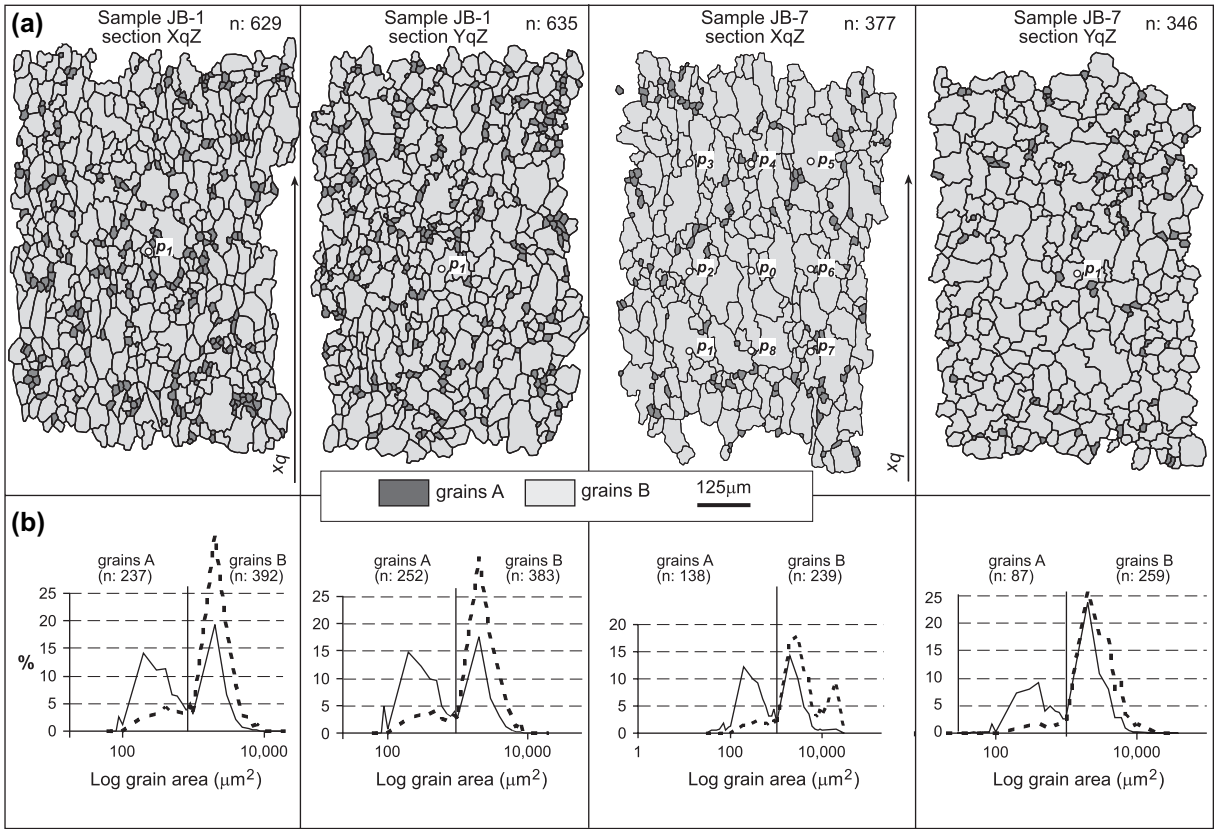

Fig. 8. Shape-fabric analysis of the Courel quartzite. (a) Grain-boundary maps for sections *XZ* and *YZ* of samples JB-1 and JB-7. Different grey tones represent quartz grains A and B discriminated from the grain size diagram. (b) Grain size diagrams showing the frequency (black line) and the area per cent (dashed line).

3.4. Analysis of kinematical folding mechanisms in minor folds

Certain geometrical features of folds, such as the morphology of the folded surface and layer profile or the angular relationship between bedding and cleavage, can be used to gain insight into the kinematic mechanisms that produced them. In this respect, the program FoldModeler (Bobillo-Ares et al., 2004), which generates theoretical folds applying the transformation equations corresponding to different folding mechanisms to an initial net of parallelograms (Bastida et al., 2005), is a powerful tool. The FoldModeler version used in this paper allows modelling of folds by tangential longitudinal strain without area change, tangential longitudinal strain with area change (Bobillo-Ares et al., 2006), flexural flow, and the superposition of a general homogeneous strain that can be rotational or irrotational and whose principal directions can have any orientation with respect to the geometrical elements of the fold. The incorporation of this strain, in general, produces asymmetric folds and represents the main difference with the previous 'FoldModeler'. The mechanisms can be applied in any order. Comparison of the geometrical features of the modelled folds with those observed on minor folds of the Courel recumbent syncline sheds light on the more probable sequences of folding mechanisms that could produce these folds.

Several metre and hectometre scale D_1 folds were studied in the field in order to obtain structural data, and nine were selected for quantitative analysis using FoldModeler. All these folds are located at or near the hinge zone of the Courel recumbent syncline (Figs. 2, 5 and 6). These folds are class 1C (Fig. 13) and show convergent cleavage patterns that approach an axial plane distribution in the less competent layers. All these characteristics have been used for the fit with theoretical folds. The $\phi - \alpha$ graphs show the variation of the cleavage inclination (ϕ) vs. bedding inclination (α) on the fold profile (Fig. 12). The cleavage pattern is represented in the $\phi - \alpha$ graph as a set of points that show an increasing trend (Fig. 12), although the point dispersion is very high in some cases.

A good theoretical fit of all the features observed in the natural folds is very difficult, especially in the cases with a high dispersion of data in the $\phi - \alpha$ graphs (Figs. 12–14). Nevertheless, the sequence of folding mechanisms that gives the best fits to the folds analysed begins with an episode of layer shortening without area change and with $\sqrt{\lambda_3} = 0.8$, followed by events of: (i) equiareal tangential longitudinal strain, (ii) tangential longitudinal strain with area change, and (iii) flexural flow. The intensities of these three mechanisms vary in the folds analysed (Table 1), and it is observed that the equiareal tangential longitudinal strain and tangential longitudinal strain with area change intensities (measured as increments in the normalized amplitude, Δh) are similar, with each of them approximately doubling the flexural flow intensity. In most cases, the fold is approximately parallel after

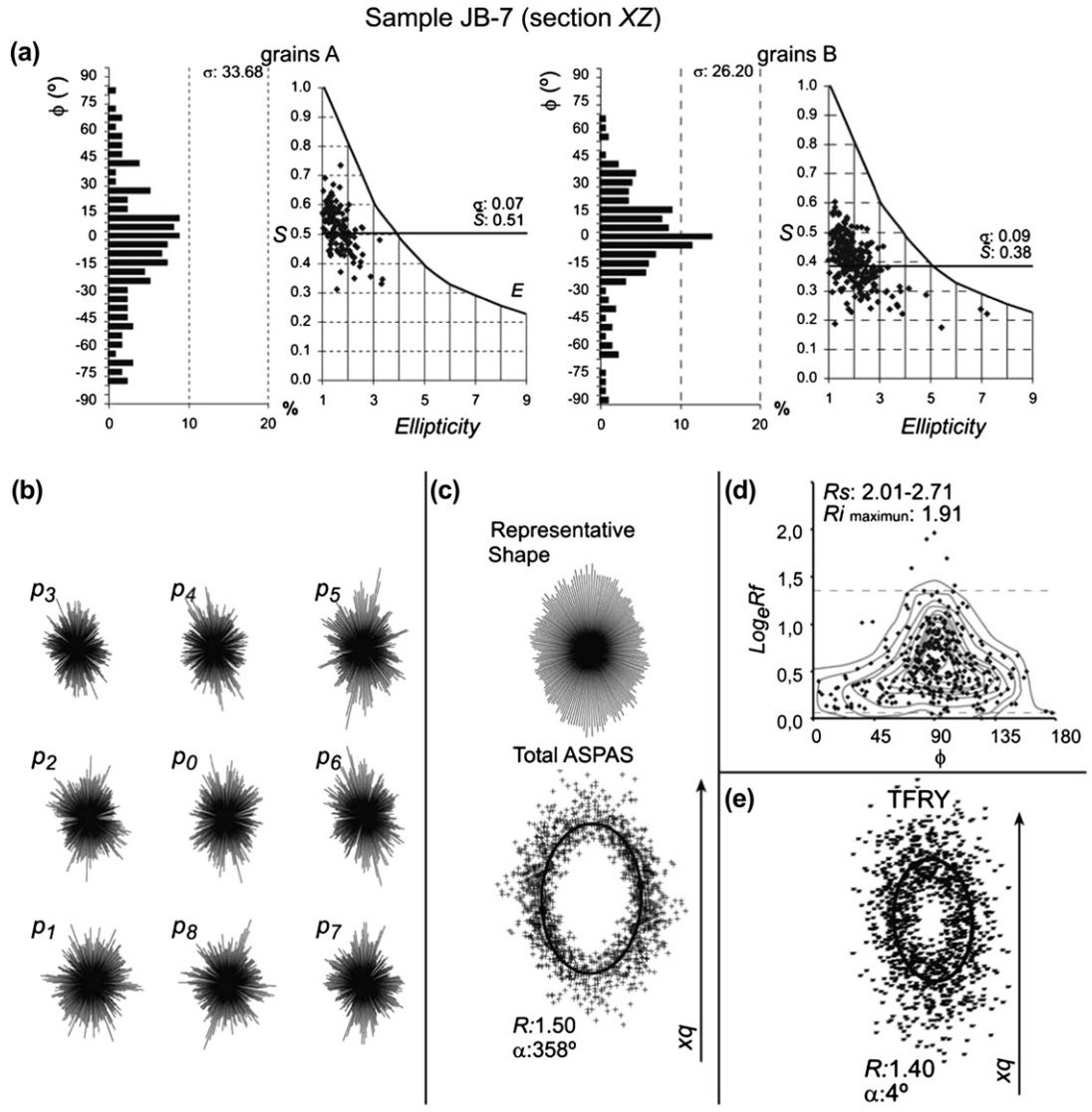

Fig. 9. Shape-fabric analysis of sample JB-7 (from Fernández et al., 2005, Fig. 5). (a) Histograms showing the frequency of the orientation (ϕ) of the major ellipse inscribed in each grain for grains A and B, and diagrams of the shape parameter (S) vs. ellipticity for grains A and B; σ is the standard deviation, $\overline{S}$ is the arithmetic mean of S (horizontal black line). (b) Individual ASPAS diagrams calculated for the nine centres p_i shown in Fig. 8a. (c) Representative shape and total ASPAS diagrams. (d) R_f/ϕ diagram. Dashed lines represent the R_f maximum and minimum calculated following the same procedure that of Ramsay and Huber (1983, p. 83). (e) TFry analysis plot.

the application of these mechanisms. The sequence finishes with an event of homogeneous flattening with $\sqrt{\lambda_3}$ between 0.6 and 0.7. The theoretical folds generated by this combination of mechanisms show R_s (in this case $R_s = \sqrt{\lambda_2/\lambda_3}$) values between 1.9 and 2.8 in the hinge zone outer arc, whereas for the inner arc R_s values range between 3 and 6.3 (Table 1). Fold 16 shows a protuberance in the inner arc that can be only modelled with very high R_s values. The chevron shape of fold 12 also requires R_s values higher than those found in the other folds.

4. Development of the Courel recumbent syncline

The analysis of the mechanisms involved in the development of huge recumbent folds as the Courel recumbent syncline poses a classic problem in the study of orogenic belts. The construction of a model for the development of the Courel recumbent syncline must take into account the sequence of folding mechanisms obtained using FoldModeler, the coaxial character of the last stages of the fabric evolution suggested by the quartz *c*-axis fabrics, and the approximately symmetrical character of the Courel recumbent syncline as regards the Lower Ordovician quartzite layer thickness. In addition, any evolutionary model for the Courel recumbent syncline must explain both its geometry and its recumbent attitude.

As regards the Courel recumbent syncline geometry, the folding mechanisms of the minor folds and the geometry of the cross section (Fig. 3) suggest that this syncline mainly developed by buckling plus flattening. According to the orthorhombic symmetry of the quartz *c*-axis fabrics and the

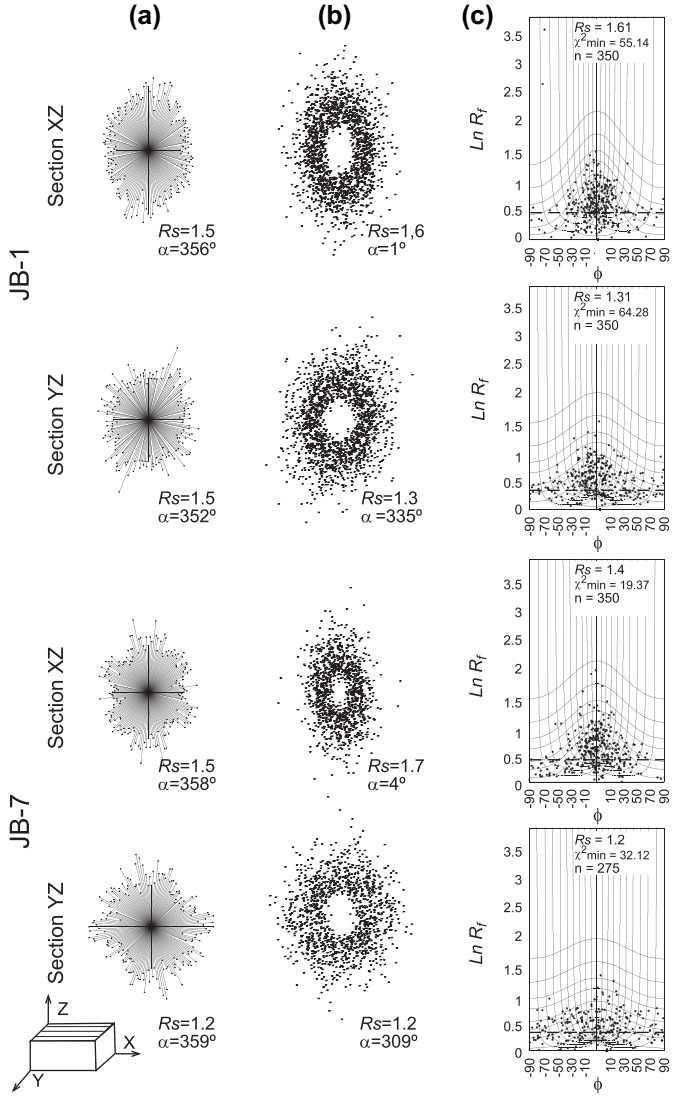

Fig. 10. Strain analysis of the Courel quartzite: (a) ASPAS diagrams of the *XZ* and *YZ* sections of samples JB-1 and JB-7. (b) TFry analysis plot for the same sections. (c) R_f/ϕ diagrams for the same sections; R is the aspect ratio of an ellipse fitted by the standard least squares method following the procedure of Fernández et al. (2005); α is the orientation of the long axis measured in anticlockwise sense from the vertical axis. R_f, R_i and R_s are the standard parameters of the R_f/ϕ method.

similar thickness of the competent layers in the two limbs, the homogeneous deformation was probably a flattening subperpendicular to the axial plane. To assess the amount of flattening and the amplitude of the buckling fold, the Srivastava and Shah (2006) method has been applied to the Armorican quartzite folded by the Courel recumbent syncline. The flattening strain ratio R obtained is about 5, and the buckling fold has a normalized amplitude of about 2.3 and a round shape.

Rotation of the axial plane is needed to explain the recumbent character of the Courel recumbent syncline. This rotation requires deformation in a non-coaxial regime. Taking into account the regional vergence of the D_1 structures towards the foreland (NNE) in the Variscan belt of the NW Spain, the rotation could occur during folding in a context of non-coaxial deformation with a dominant foreland-directed simple shear component. Other shear directions make it difficult to explain the huge extension of the area with D_1-folds in this part of the orogen. Development of buckling folds in a simple shear regime requires an obliquity between the layers and the shear direction (Ghosh, 1966; Ez, 2000; Carreras et al., 2005; among others). In this deformation regime, folds with gently inclined axial surfaces are only produced when the shear direction plunges slightly. In the study case, the two conditions are accomplished if the shear direction slightly plunges towards the hinterland and the layers gently dip towards the foreland. This involves an uplift of the hinterland that could occur at the beginning of the Variscan deformation. The uplift was probably formed as a result of D_1 deformation, which progresses from the hinterland (Central-Iberian zone) to the foreland (Cantabrian zone) (Pérez-Estaún et al., 1991; Dallmeyer et al., 1997).

From these premises, it is possible to develop an evolutionary model for the Courel recumbent syncline. The evolution starts from an initial configuration characterized by a supratenuous rollover anticline developed during the Ordovician and associated with the growth of the Villavieja fault (Fernández, 2001), located to the north of the Courel recumbent syncline (Fig. 15a). The core of the anticline with its condensed Middle and Upper Ordovician series constituted a weak zone that conditioned the location of the Courel recumbent syncline hinge when the Variscan deformation began; the evolution transformed the rollover anticline into a syncline. This change must be related to a tectonic uplift of the southern part of the study zone that gave rise to a rotation of the southern limb of the rollover anticline (Fig. 15b).

A deformation with a dominant simple shear component induced minor layer shortening, buckling and body rotation in the competent layers (Fig. 15c). Assuming a shear direction plunge of 10° towards the hinterland and a constant arc-length during buckling, a fold with a normalized amplitude of about 2.3 and the rounded shape obtained above, requires a shear strain of about 2.

After buckling, a flattening took place with a R value of about 5 and maximum shortening perpendicular to the axial plane (Fig. 15d). Assuming isochoric deformation in the quartzite and taking into account that the λ_1 direction is parallel to the fold axis, as indicated by the stretching lineation, an area decrease is required in the fold profile. Since $R \approx 5$, this area decrease must be >42%. In Fig. 15d the area decrease is close to this minimum value. Note that the λ_1 direction indicated by the stretching lineation and the boudinage is incompatible with the previous simple shear regime, and consequently this λ_1 direction must be related to flattening. Location of the Courel recumbent syncline in the subhorizontal limb of a large open asymmetric fold formed during the third phase of Variscan deformation (D_3) probably contributed to its recumbent character (Fig. 15e).

5. Discussion and conclusions

The structural analysis made in this study combines methods of strain estimation at different scales whose results

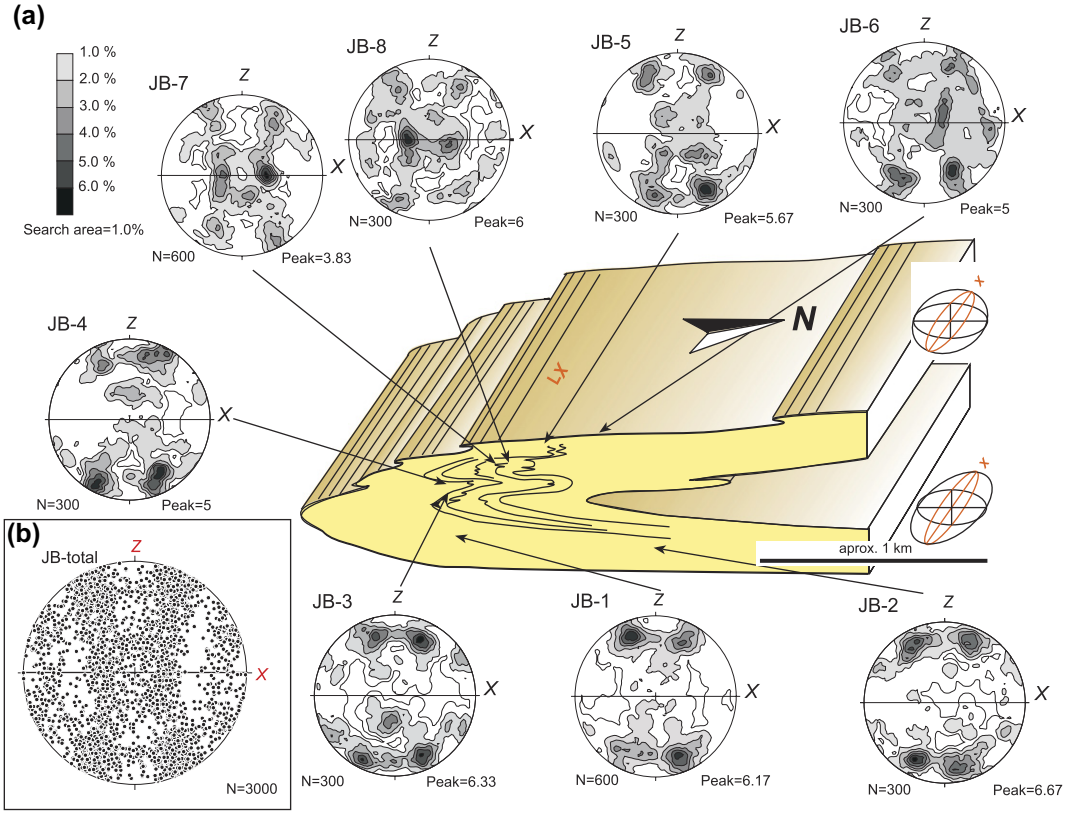

Fig. 11. (a) *c*-Axes preferred orientation of the Courel quartzite; U-stage measurements, equal-area projections; solid line: rock foliation (normal to *Z*); *X* is horizontal (lineation defined by the preferred elongation of the quartz grains within the foliation plane). (b) Full data projection. The ellipsoids on the right-hand side represent the strain ellipsoids calculated from samples JB-7 and JB-1.

pose various problems. Flattening *R* values estimated from the analysis of the major structure are higher than those obtained from the kinematical models of minor folds (Table 1), and these are higher than those obtained from the strain analysis (Figs. 9 and 10). The differences between the results of the first two methods could be due to the formation of the minor folds in a late event during the evolution of the major fold. Buckling probably still occurred in the hinge zone during the flattening stage of the major fold. On the other hand, the strain values obtained from the fabric analysis are too low when compared with those estimated by the other methods. These differences could be due to certain limitations of the fabrics when used in the strain analysis. For example, the anastomosing foliations observed in the quartzite under the microscope (Fig. 7) can have associated displacements along the cleavage domains that are not detected in the strain analysis, which assumes a continuous medium. As a result, the *R* values obtained in the strain analysis are minimum values, and can be lower than those obtained from the other methods.

The kinematical models for the minor folds of the Courel recumbent syncline involve a sequence of initial layer shortening ($\sqrt{\lambda_3} = 0.8$), followed by tangential longitudinal strain and flexural flow in such a manner that the former produces an amplification of the structure (Δh) approximately four times that of the latter (Table 1). Tangential longitudinal strain and flexural flow characterized a buckling process that probably also involved a rotation of the fold axial plane, together with the major fold, towards an attitude moderately dipping to the south, in a progressive evolution towards the actual recumbent position (Fig. 3). The last folding event was a fold flattening with a mean value of $R \approx 2$ (Table 1), which in the modelled folds involved maximum stretch perpendicular or slightly oblique to the axial plane. This sequence of shortening + buckling + flattening was produced in the hinge zone of the Courel recumbent syncline. A feature of these folds is the dominantly coaxial character of the flattening, whose maximum shortening direction is nearly perpendicular to the axial plane. This agrees with the orthorhombic symmetry of the quartz *c*-axis fabrics. In addition, superposition to the modelled buckle folds of a homogeneous non-coaxial strain gives rise to asymmetric geometries that do not resemble those of the natural folds analysed. Minor folds analysed are located at or near the hinge zone of the Courel recumbent syncline and generally show a higher interlimb angle than this major fold. These data confirm that the minor folds were formed in an advanced stage during the evolution of the Courel recumbent syncline.

The evolution of the major fold involved (Fig. 15): (a) development of a supratenuous rollover anticline during the Ordovician, related to the Villavieja fault; (b) tectonic uplift of the southern part of the section giving rise to a generalized dip of the layers towards the foreland; (c) minor layer shortening, buckling and rotation in a simple shear regime with a shear direction foreland directed and gently plunging towards the

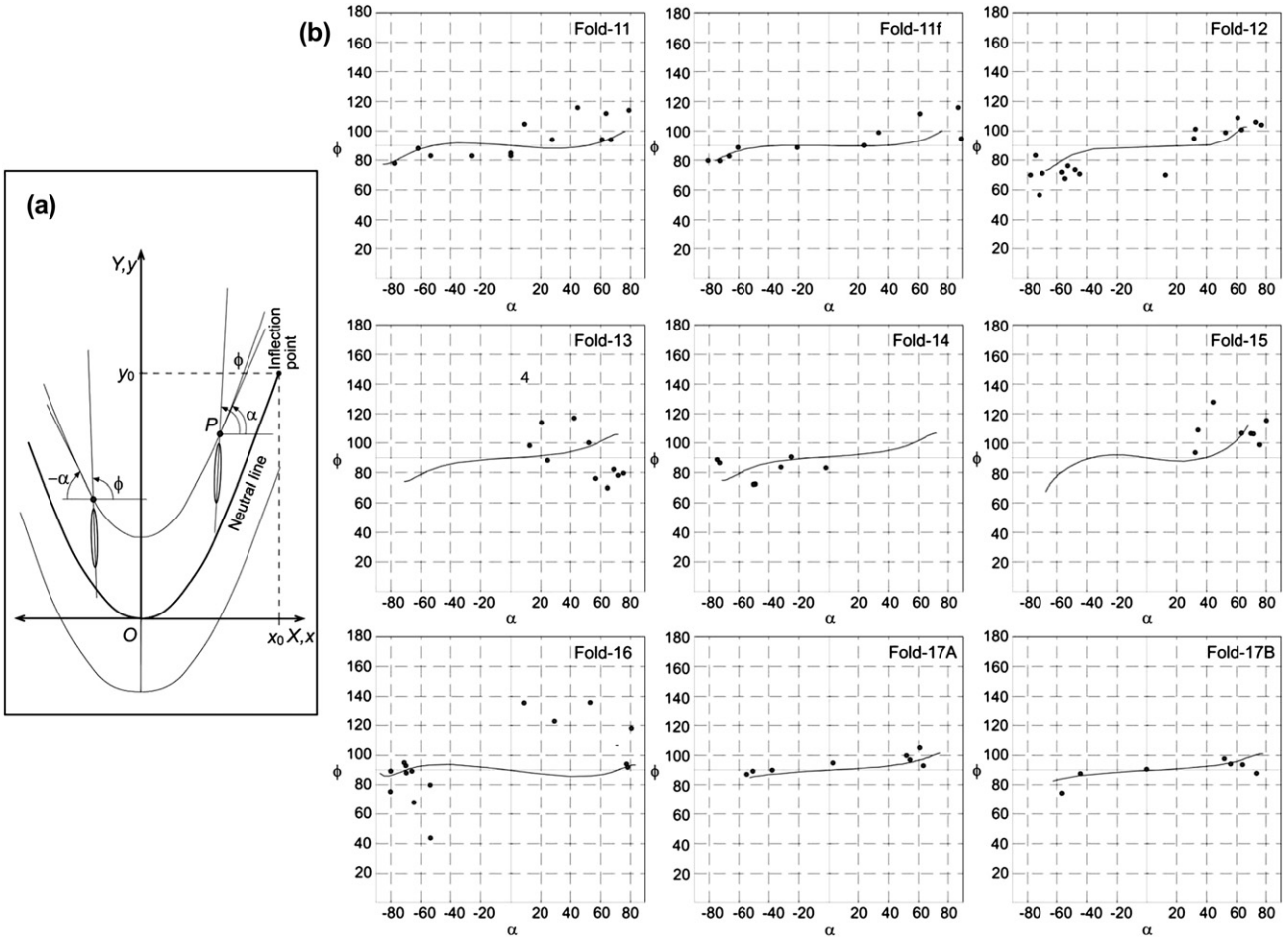

Fig. 12. (a) Definition of angles ϕ and α. (b) $\phi - \alpha$ diagrams showing the data from the natural folds (points) and the theoretical models (solid line).

hinterland; (d) flattening with the maximum shortening direction steeply inclined, and involving an important area decrease in the profile plane; stages (b)–(d) correspond to the development of D_1 of the Variscan deformation; and (e) D_3 folding and rotation to the recumbent present position.

The evolution described above involves a transition from a non-coaxial regime to a flattening with a very steep maximum shortening direction. This transition can be tentatively related to an increasing influence of gravity as a consequence of the tectonic superposition due to folding. The gravity impact on the development of recumbent folds has been commented by several authors (Bucher, 1956, 1962; Hudleston, 1977; Vacas Peña and Martínez Catalán, 2004; among others).

Recumbent folds induced by simple shear have been theoretically or experimentally analysed by several authors (Hudleston, 1977; Sanderson, 1979; Ez, 2000; Carreras et al., 2005; among others). This type of model has been applied to the case of the Helvetic fold-thrust belt by Ramsay et al. (1983). Independent of the active or passive behaviour of the layer, the formation of recumbent folds by this mechanism requires a large amount of shear or a high dip of the layers towards the shear direction. None of these conditions are accomplished in the case of the Courel recumbent syncline. Ez (2000) and Carreras et al. (2005) have also analysed the formation of recumbent folds by superposition of simple shear and pure shear. Dietrich and Casey (1989) have described a model involving combination of simple shear and a variable amount of pure shear to explain the structure of the Helvetic nappes and the very steep gradients of increasing strain towards the root of the nappes. These models allow the formation of recumbent folds with lower strain amounts or lower initial dip of the layers towards the shear direction than the

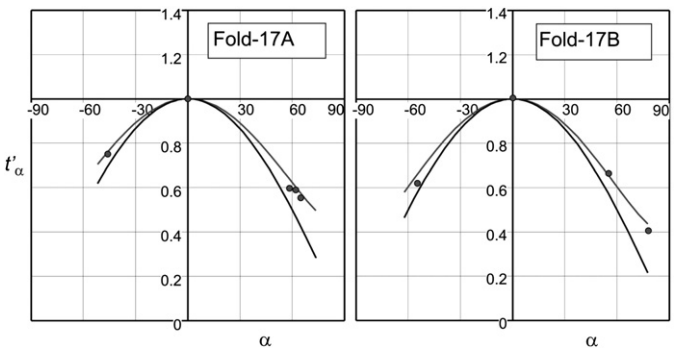

Fig. 13. Ramsay classification of folds 17A and 17B showing the values obtained from the natural folds (points) and the theoretical models (solid lines).

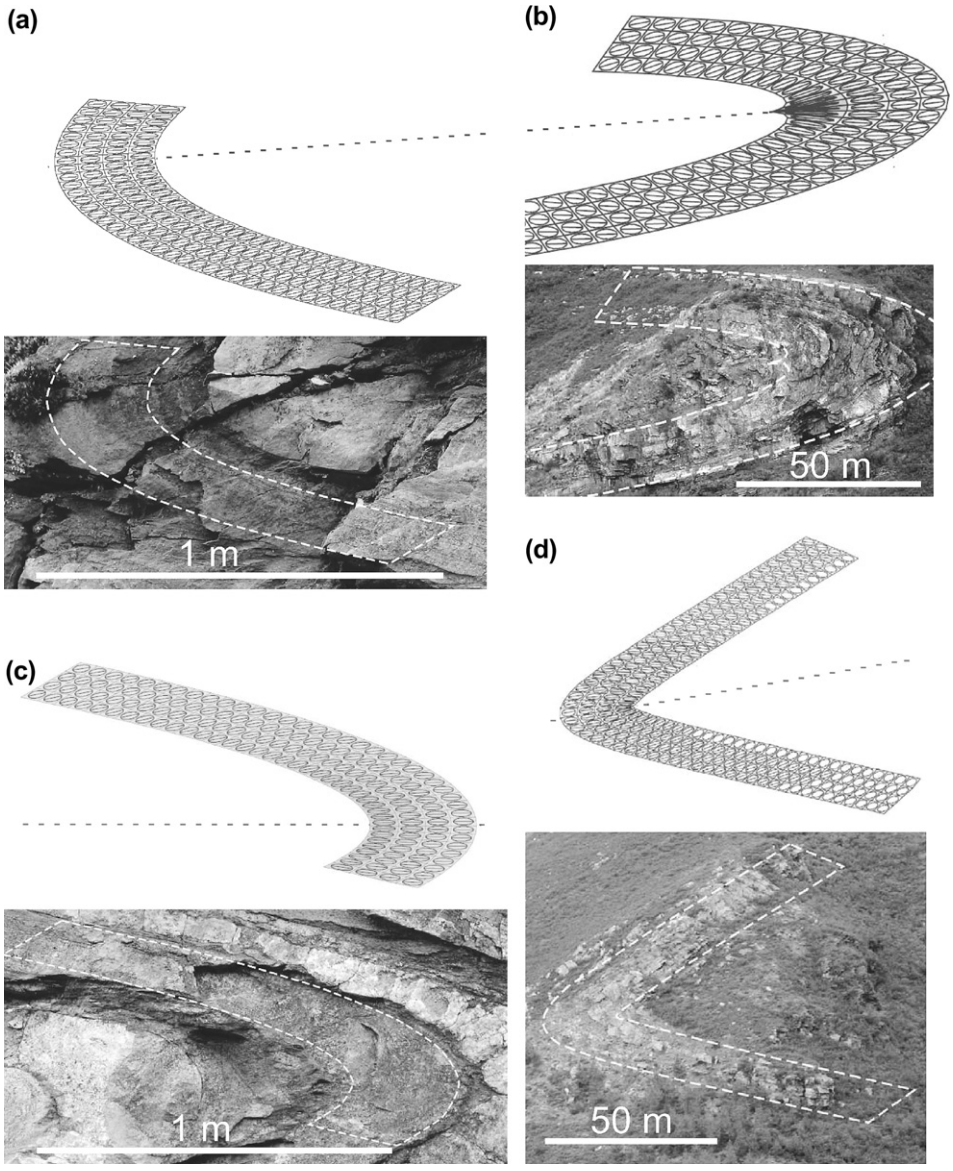

Fig. 14. Some representative examples of fit between the natural and the theoretical folds, defined by the result of deformation of an initial net of quadrilaterals showing the strain ellipses and their major axes. (a) Fold 11. (b) Fold 12. (c) Fold 16. (d) Fold 17A. (e) Fold 17B.

Table 1
Magnitude of the different kinematical mechanisms and R maximum values for the inner (IA) and the outer arc (OA) for the theoretical fold models

Fold ref.	ILSH ($\sqrt{\lambda_2}$)	DLTE (Δh)	DLTP (Δh)	FF (Δh)	FL ($\sqrt{\lambda_2}$)	$R_{\mathrm{IA\ max}}$	$R_{\mathrm{OA\ max}}$
11	0.8	0.4	0.35	0.2	0.71	5.2	1.9
11f	0.8	0.4	0.4	0.2	0.67	4.5	2.5
12	0.8	0.3	0.6	0.16	0.67	6.3	1.85
13	0.8	0.4	0.5	0.2	0.71	4.5	2
14	0.8	0.4	0.5	0.2	0.71	4.5	2
15	0.8	0.4	0.4	0.3	0.8	3	1.6
16	0.8	1	0.2	0.1	0.58	2515	2.1
17A	0.8	0.4	0.2	0.2	0.65	4.2	2.8
17B	0.8	0.4	0.4	0.2	0.62	5.2	2.8

Kinematical mechanisms are: LS: layer shortening, ETLS: equiareal tangential longitudinal strain, PTLS: parallel tangential longitudinal strain, FF: flexural flow and HF: homogeneous flattening.

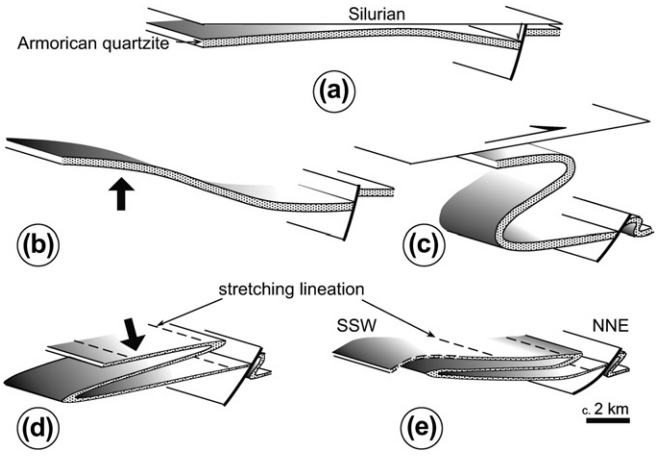

Fig. 15. Synthetic kinematical model for the Courel recumbent syncline. For explanation, see text.

simple shear models, and resemble the one proposed here for the Courel recumbent syncline. Nevertheless, the geometry of the Courel recumbent syncline suggests that flattening is approximately homogeneous throughout the fold. A different model is that of Bell and Hickey (1998) and Bell et al. (2003), who proposed the formation of recumbent folds in Mount Isa region (Australia) by rotation of previous right folds during an episode of subhorizontal shear. This evolution involves a poliphasic deformation with superposition of microstructural events that is not observed in the Courel recumbent syncline.

Acknowledgements

The present work was supported by Spanish CGL2005-02233-BTE project funded by Ministerio de Educación y Ciencia and Fondo Europeo de Desarrollo Regional (FEDER). We are grateful to T.H. Bell and one anonymous reviewer for many valuable suggestions that notably improved the manuscript.

References

Abril-Hurtado, J., 1979. Mapa Geológico Nacional E. 1: 50.000, Hoja 157 (Oencia), IGME, Madrid.

Bastida, F., 1980. Las estructuras de la primera fase de deformación herciniana en la Zona Asturoccidental-leonesa (Costa cantábrica, NW de España). Unpublished Ph.D thesis, Universidad de Oviedo, 276 pp.

Bastida, F., Pulgar, J.A., 1978. La estructura del manto de Modoñedo entre Burela y Tapia de casariego (Costa Cantábrica, NW de España). Trabajos de Geología de la Universidad de Oviedo 10, 75–159.

Bastida, F., Martínez-Catalán, J.R., Pulgar, J.A., 1986. Structural, metamorphic and magmatic history of the Mondoñedo nappe (Hercynian belt, NW Spain). Journal of Structural Geology 8, 415–430.

Bastida, F., Aller, J., Bobillo-Ares, N.C., Toimil, N.C., 2005. Fold geometry: a basis for their kinematical analysis. Earth-Science Reviews 70, 129–164.

Bell, T.H., Hickey, K.A., 1998. Multiple deformations with successive subvertical and subhorizontal axial planes in the Mount Isa region: their impact on geometric development and significance for mineralization and exploration. Economic Geology 93, 1369–1389.

Bell, T.H., Ham, A.P., Hickey, K.A., 2003. Early formed regional antiforms and synforms that fold younger matrix schistosities: their effect on sites of mineral growth. Tectonophysics 367, 253–278.

Bobillo-Ares, N.C., Bastida, F., Aller, J., 2000. On tangential longitudinal strain folding. Tectonophysics 319, 53–68.

Bobillo-Ares, N.C., Toimil, N.C., Aller, J., Bastida, F., 2004. FoldModeler: a tool for the geometrical and kinematical analysis of folds. Computers and Geosciences 30, 147–159.

Bobillo-Ares, N.C., Aller, J., Bastida, F., Lisle, R.J., Toimil, N.C., 2006. The problem of area change in tangential longitudinal strain folding. Journal of Structural Geology 28, 1835–1848.

Borradaile, G.J., Bayly, M.B., Powell, C.M.A., 1982. Atlas of Deformational and Metamorphic Rock Fabrics. Springer-Verlag, Berlin Heidelberg, New York, 551 pp.

Bouchez, J.L., Mainprice, D.H., Trepied, L., Doukhan, J.C., 1984. Secondary lineation in a high-T quartzite (Galicia, Spain): an explanation for an abnormal fabric. Journal of Structural Geology 6, 159–165.

Bucher, W.H., 1956. Role of gravity in orogenesis. Bulletin of the Geological Society of America 67, 1295–1318.

Bucher, W.H., 1962. An experiment of the role of gravity in orogenic folding. Geologische Rundschau 52, 804–810.

Carreras, J., Druget, E., Griera, A., 2005. Shear zone-related folds. Journal of Structural Geology 27, 1229–1251.

Chew, D.M., 2003. An Excel spreadsheet for finite strain analysis using the R_f/ϕ technique. Computers and Geosciences 29, 295–299.

Dallmeyer, R.D., Martínez-Catalán, J.R., Arenas, R., Gil-Ibarguchi, J.I., Gutiérrez-Alonso, G., Farias, P., Bastida, F., Aller, J., 1997. Diacronous variscan tectonothermal activity in the NW Iberian massif: evidence from $^{40}Ar/^{39}Ar$ dating of regional fabrics. Tectonophysics 277, 307–337.

Dietrich, D., Casey, M., 1989. A new tectonic model for the Helvetic mappes. In: Coward, M.P., Dietrich, D., Park, R.G. (Eds.), Alpine Tectonics. Geological Society of London, Special Publications, vol. 45, pp. 47–63.

Dunnet, D., 1969. A technique of finite strain analysis using elliptical particles. Tectonophysics 7, 117–136.

Exner, H.E., 1972. Analysis of grain- and particle-size distribution in metallic materials. International Metallurgical Review 159, 25–42.

Ez, V., 2000. When shearing is a cause of folding. Earth-Science Reviews 51, 155–172.

Fernández, F.J., 2000. Meso and microstructural analysis of the Villavieja Fault and their kinematic interpretation. In: Variscan-Appalachian Dynamics: The Building of the Upper Paleozoic Basement. Basement Tectonics 15, pp. 221–225 (A coruña, Spain, Program and Abstracts, 7).

Fernández, F.J., 2001. Características estratigráficas y estructurales del margen noroccidental del sinclinorio de Truchas: geología aplicada a la prospección y explotación de pizarras de techar. Revista de la Sociedad Geológica de España 14, 161–173.

Fernández, F.J., Menéndez-Duarte, R., Aller, J., Bastida, F., 2005. Application of geographical information systems to shape-fabric analysis. In: Bruhn, D., Burlini, L. (Eds.), High-Strain Zones: Structure and Physical Properties. Geological Society of London, Special Publications, vol. 245, pp. 409–420.

Fry, N., 1979. Random point distribution and strain measurement in rocks. Tectonophysics 60, 89–105.

Ghosh, K.S., 1966. Experimental tests of buckling folds in relation to strain ellipsoid in simple shear deformations. Tectonophysics 3, 169–185.

González-Lodeiro, F., Iglesias-Ponce de León, M., 1978. Mapa Geológico Nacional E. 1:50.000, Hoja 156 (Monforte de Lemos) y memoria explicativa. IGME, Madrid.

Hirth, G., Tullis, J., 1992. Dislocation creep regimes in quartz aggregates. Journal of Structural Geology 14, 145–159.

Hudleston, P.J., 1977. Similar folds, recumbent folds, and gravity tectonics in ice and rocks. Journal of Geology 85, 113–122.

Lisle, R.J., 1985. Geological Strain Analysis. A Manual for the R_f/ϕ Technique. Pergamon Press, Oxford, 99 pp.

Lister, G.S., Hobbs, B.E., 1980. The simulation of fabric development during plastic deformation and its application to quartzite: the influence of deformation history. Journal of Structural Geology 2, 355–370.

Marcos, A., 1973. Las series del Paleozoico inferior y la estructura herciniana del occidente de Asturias (NW de España). Trabajos de Geología de la Universidad de Oviedo 6, 3–113.

Martínez, F.J., Carreras, J., Arboleya, M.L., Dietsch, C., 1996. Structural and metamorphic evidence of local extension along the Vivero fault coeval with bulk crustal shortening in the Variscan chain (NW Spain). Journal of Structural Geology 18, 61–73.

Martínez-Catalán, J.R., 1985. Estratigrafía y estructura del Domo de Lugo (Sector Oeste de la Zona Asturoccidental-leonesa). Corpus Geologiae Gallaeciae 2 (2ª Serie), 1–291.

Matte, P., 1968. La structure de la virgation hercynienne de Galice (Espagne). Extrait des travaux du laboratoire de géologie de la Faculté des Sciences de Grenoble 44, 1–128.

Pérez-Estaún, A., 1978. Estratigrafía y estructura de la rama S. de la Zona Asturoccidental-Leonesa. Memorias del IGME 92, 152 (Madrid).

Pérez-Estaún, A., Martínez-Catalán, J.R., Bastida, F., 1991. Crustal thickening and deformation sequence in the footwall to the suture of the Variscan belt of northwest Spain. Tectonophysics 191, 243–253.

Powell, C.M.A., 1979. A morphological classification of rock cleavage. Tectonophysics 58, 21–34.

Pulgar, J., 1980. Análisis e interpretación de las estructuras originadas durante las fases de replegamiento en la Zona Asturoccidental-leonesa (Cordillera Herciniana, NW de España). Unpublished Ph.D thesis, Universidad de Oviedo, 334 pp.

Ramsay, J.G., 1967. Folding and Fracturing of Rocks. McGraw-Hill, New York, 568 pp.

Ramsay, J.G., Huber, M.I., 1983. In: Strain Analysis. The Techniques of Modern Structural Geology, vol. 1. Academic Press, London, p. 307.

Ramsay, J.G., Casey, M., Kligfield, R., 1983. Role of shear in development of the Helvetic fold-thrust belt of Switzerland. Geology 11, 439–442.

Rich, J.L., 1934. Mechanics of low-angle overthrust faulting as illustrated by Cumberland thrust bock. Virginia, Kentucky and Tennessee. Bulletin of the American Association of Petroleum Geology 18, 1584–1596.

Riemer, W., 1963. Eutwicklung des Paläozoikums in der südlichen Provinz Lugo. Neues Jurburch für Geologie und Paläontologie Abhundlungen 117, 273–285.

Sanderson, D.J., 1979. The transition from upright to recumbent folding in the Variscan fold belt of southwest England: a model based on the kinematics of simple shear. Journal of Structural Geology 1, 171–180.

Sanderson, D.J., 1982. Models of strain variation in nappes and thrust sheets: a review. Tectonophysics 88, 201–233.

Schmid, S.M., Casey, M., Starkey, J., 1981. An illustration of the advantages of a complete texture analysis described by the orientation distribution function (ODF) using quartz pole figure data. Tectonophysics 78, 101–117.

Srivastava, D.C., Shah, J., 2006. A rapid method for strain estimation from flattened parallel folds. Journal of Structural Geology 28, 1–8.

Vacas Peña, J.M., Martínez Catalán, J.R., 2004. A computer program for the simulation of folds of different sizes under the influence of gravity. Computers and Geosciences 30 (2004), 33–43.